GEOLOGY

Tephra seismites—Understanding seismic hazard of hidden faults by analyzing liquefied tephra layers in lakes

Max O. Kluger[1]*, Richard A. Melchert[1,2], José M. Moratalla[2], Tehnuka Ilanko[1,3], David J. Lowe[1], Vicki G. Moon[1], Pilar Villamor[2], Jordanka Chaneva[1,4], Nic Ross[5], Rolando P. Orense[6]

Assessing seismic hazards in regions with hidden or poorly expressed faults is one of the major challenges in paleoseismology today. Here, we used computed tomography imaging to quantify the dimensions and distribution of liquefaction structures in ≤17.5–thousand-year-old tephra layers in 18 lakes scattered across the poorly expressed Hamilton Basin fault system in northern New Zealand. These "tephra seismites," embedded in unconsolidated, organic-bearing lake sediment, increase in occurrence and dimensions toward known faults and indicate the occurrence of a local hidden fault segment. Through incorporating peak ground acceleration modeling, we found that the spatial distribution of tephra seismites directly relates to the ground shaking induced by near-field fault ruptures. We used the variability in tephra seismites within the stratigraphic record and tephrochronology to better constrain the recurrence intervals and magnitudes of paleoearthquakes from both the Hamilton Basin and adjacent Hauraki Basin fault systems. Our methodology is globally applicable in volcanic and tectonic regions where liquefaction structures are preserved among (hidden) faults.

INTRODUCTION

Hidden faults, which are of particular concern because of their undeterminable potential to induce seismic events, have been identified beneath numerous urbanized areas, including those in Los Angeles, Portland, and Christchurch (*1*–*4*). The 2011 Canterbury and 1897 Assam earthquakes are notable examples of this phenomenon, as both events occurred because of the rupture of hidden faults (*5*, *6*). In regions characterized by hidden or poorly expressed faults, the reconstruction of paleoearthquakes is commonly based on turbidite paleoseismology (*7*) or earthquake-induced soft-sediment deformation structures (i.e., seismites) (*8*, *9*). Most knowledge regarding seismites is derived from field studies of lithified sediments accessible through outcrops, trenches (*10*–*13*), and cores (*14*). Consequently, the dimensions and types of seismites depend on the distance of paleoearthquakes and the intensity of shaking at the liquefaction site (*15*, *16*). Notable challenges arise when using lithified sediments for paleoseismic assessments. The process of diagenesis may induce compaction and cementation within seismites, altering their morphology, dimensions, and material properties. In addition, in most paleoseismology studies, only a handful of field sites were normally available for the characterization of seismites, this paucity being identified as an important barrier to comprehensive spatial and temporal earthquake reconstructions (*17*).

Unlithified seismites offer numerous advantages in paleoseismology. In the absence of substantial diagenetic imprinting, the study of unlithified seismites preserved in extant lake sediments can provide a less-biased understanding of the liquefaction process that led to their formation (*18*–*20*). Noteworthy examples of unlithified seismites in lakes or shallow basins have been documented in several locations, including Lake Riñihue in Chile (*21*), central Switzerland (*22*), north Iceland (*23*), the Dead Sea (*24*), and the Hamilton lowlands in northern New Zealand (*20*). The three-dimensional morphologies of seismites from Lake Riñihue and from lakes within the Hamilton lowlands have been visualized through the application of x-ray computed tomography (CT). These studies used tephrochronology to establish a correlation between seismite occurrence and paleoearthquakes (*25*). However, the dimensions and distribution of these seismites were not used for spatial or temporal earthquake reconstruction.

The aim of our study is to enhance the reconstruction of seismic events from hidden faults by analyzing the dimensions and spatial-temporal distribution of soft-sediment deformation structures that occur in thin, distal lacustrine tephra layers (i.e., tephra seismites) via CT imaging. Tephra is the explosively erupted, unconsolidated product of a volcanic eruption of any grain size (including volcanic ash) or composition (*26*). The ≤17.5–thousand year (ka)–old tephra seismites presented in our study are embedded in organic-bearing lake sediment and are present in at least 18 lakes distributed across the poorly expressed Hamilton Basin fault system in northern New Zealand (*20*, *27*) (Fig. 1A). The seismic activity of the Hamilton Basin faults, parts of which lie underneath a large urban area (Hamilton City, population ~200,000), is unknown. In relatively close proximity, the active Kerepehi and Te Puninga faults in the nearby Hauraki Basin (~20 to 60 km to the northeast) have likely produced moment magnitude (M_w) 6.9+ earthquakes with recurrence intervals between 3 and 15 ka based on paleoseismic studies (Fig. 1B) (*28*, *29*). The activity of the Aka Aka–Pōkeno–Mangatangi fault system (~50 to 90 km to the north) is also unknown (*30*). The tephra seismites vary in morphology and dimensions between lakes and within the stratigraphic sequence. The Hamilton lowlands, hosting the Hamilton Basin fault system, and its many lakes, are therefore considered an ideal "paleoseismograph" for reconstructing paleoearthquakes from hidden faults.

Here, we obtained medical CT images of 60 sediment cores and visualized more than 100 tephra seismites with the objective of obtaining interpolation maps of their spatial occurrence and variability in dimensions. We also analyzed their temporal variability within the stratigraphic sequence mainly using tephrochronology (supported by

[1]School of Science/Te Aka Mātuatua, University of Waikato, Hamilton 3216, New Zealand. [2]GNS Science, Lower Hutt 5011, New Zealand. [3]Royal Society Te Apārangi, Wellington 6011, New Zealand. [4]Tonkin & Taylor, Auckland 1010, New Zealand. [5]I-MED Hamilton Radiology, Hamilton 3204, New Zealand. [6]Department of Civil and Environmental Engineering, University of Auckland, Auckland 1010, New Zealand.
*Corresponding author. Email: max.kluger@waikato.ac.nz

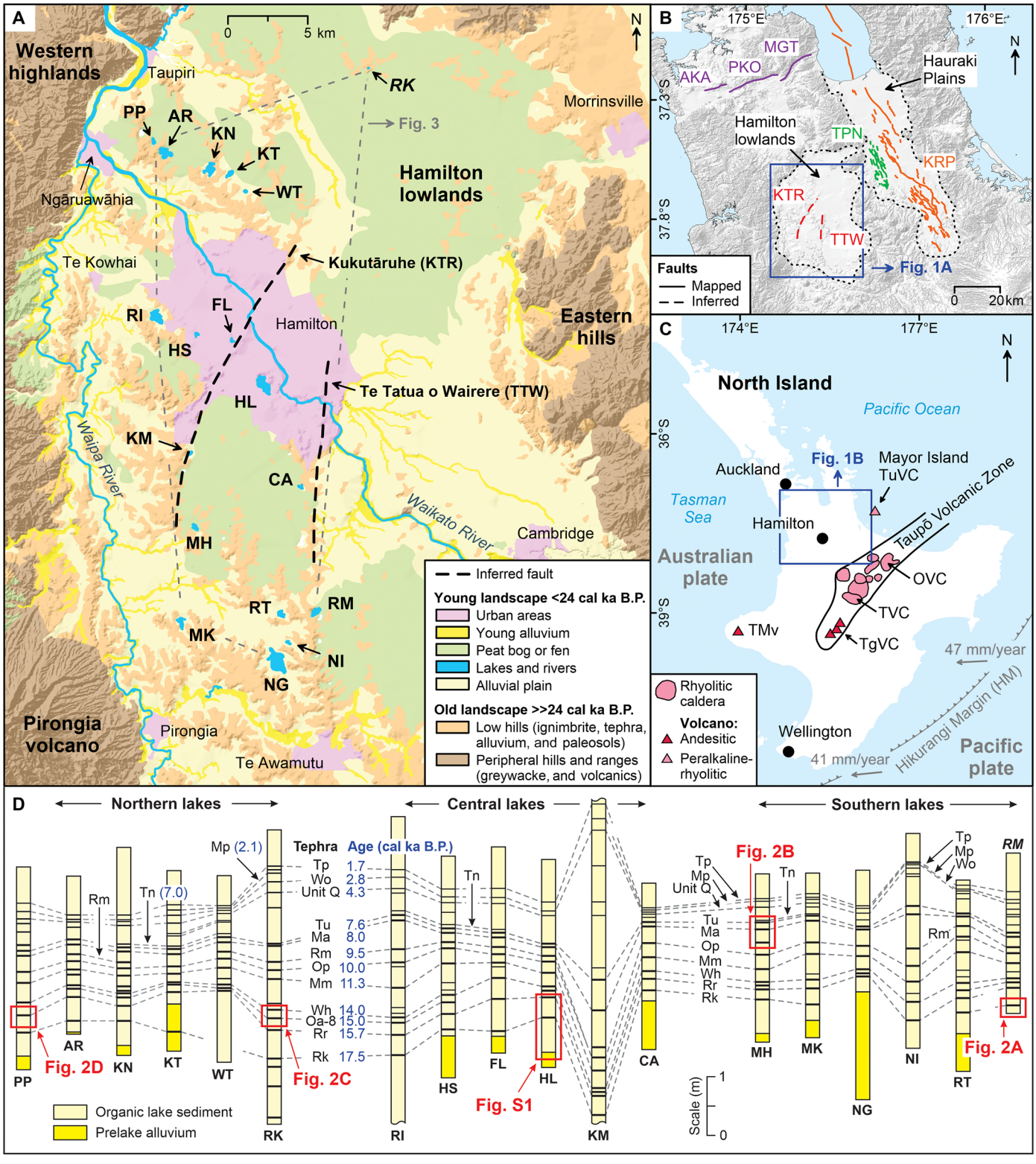

Fig. 1. Sedimentological and tectonic setting of the Hamilton lowlands. (**A**) Locations of the 18 lakes cored in this study and recently identified, poorly characterized Kūkūtāruhe (KTR) and Te Tātua ō Wairere (TTW) faults (*30*) in the Hamilton lowlands. (**B**) Wider view of the study area showing faults in the Hamilton lowlands (A), the Te Puninga (TPN) and Kerepehi (KRP) faults in the adjacent Hauraki Plains (*29*), and the Aka Aka (AKA), Pōkeno (PKO), and Mangatangi (MGT) faults to the north in the South Auckland area (*30*). (**C**) Map of the North Island, New Zealand, showing tectonic setting and major volcanic centers active since 20 cal ka B.P. (*74*). (**D**) Correlation of the sedimentary sequences, including prominent post–20-cal-ka tephra layers, between northern, central, and southern lakes within the Hamilton lowlands. Full lake names, tephra names, and volcanic sources are provided in tables S1 and S2.

radiocarbon dating, not reported) and linked these spatial-temporal liquefaction patterns to peak ground acceleration maps from rupture modeling of relevant near-field and far-field fault systems. The findings of our study are applicable in other seismically and volcanically active regions worldwide, particularly in cases where active faults are hidden or where on-fault paleoseismic studies are impracticable, and where the geological setting favors the deposition of tephras in lakes.

RESULTS AND DISCUSSION

Tephra seismites in lakes function as natural paleoseismograph

The Hamilton lowlands contain 35 extant riverine and riverine-phytogenic lakes, 18 of which were considered in our study (Fig. 1A). The sedimentary sequence of the lakes is composed of two primary geological units, namely, Late Pleistocene [greater than approximately 20 thousand calibrated years before present (20 cal ka B.P.)] prelake volcanogenic alluvial deposits (*31*), overlain by lake sediment composed of organic-bearing, unlithified, low-density silt interlayered with tephra-fall deposits (Fig. 1D) (*20*, *27*). A total of 14 prominent tephra layers, with ages ranging from 17.5 to 1.7 cal ka B.P. and thicknesses measuring between 0.2 and 8.2 cm, were identified. These layers were then correlated between lakes through tephrochronology, as detailed in table S2. Each of the tephras is consistent in its mineralogical assemblages (dominated by volcanic glass, both vesicular and nonvesicular, with subordinate felsic and mafic minerals) across the lakes in the Hamilton lowlands (*20*, *27*). This lack of spatial variability in mineralogical assemblages is anticipated, given that these are distal tephra-fall beds deposited more than 100 km from their source vents (*32*). The tephra deposits under consideration here commonly comprise horizontally bedded layers with distinct boundaries with under- and overlying organic lake sediments. The layers frequently exhibit an upper bed of silt-sized tephra, typically up to several millimeters thick. The upper silt bed is underlain by coarser tephra beds, the number and grain size of which vary between tephra layers. The upper silt bed has been classified as nonliquefiable, while the underlying beds, typically fine to medium sands, are liquefiable on the basis of their grain size distribution and cyclic triaxial testing (*19*, *20*). Most of the tephra layers (including their internal beds) exhibit minimal variability in tephra thickness and grain size across the study area, with the exception of two layers, where higher variability in tephra thickness was observed (*20*). Correlations between tephra thickness and grain size demonstrate that tephra thickness does not affect grain size properties. Consequently, tephra thickness does not influence whether or not liquefaction occurs (*20*).

We visualized a total of 346 tephra layers via CT imaging, 127 of which exhibited soft-sediment deformation structures with variable morphology and dimensions (Fig. 2 and data S1). The soft-sediment deformation structures are composed of tephra material that is emplaced downward beneath the tephra layer into the underlying organic lake sediment, forming load structures (*33*), and resembling downward-directed injectites or dykes (*11*, *14*, *20*, *34*–*37*). The longitudinal and cross-sectional CT slices and three-dimensional CT volumes provided a unique view of the load structures' morphologies, ranging from predominantly straight, elongated features (Fig. 2, A and D) to complex networks of irregular structures (Fig. 2, B and C). Individual load structures frequently intersected with one another (Fig. 2, A to C) yet at times manifested as solitary features (Fig. 2D).

The load structures observed in the Hamilton lowlands have been interpreted as the result of seismically induced liquefaction in a sedimentary system of density instability (*20*). Liquefaction was typically initiated within the central part of the tephra layer (Fig. 2D), consisting of liquefiable fine to medium sand-sized pumiceous glass particles (*18*, *38*). The liquefied material was emplaced downward mainly because of an inverse density gradient (*33*) between the tephra layers and the underlying low-density organic lake sediment underneath and partly because the nonliquefiable silty cap on the tephra layers prevented upward movement of liquefied tephra material (*20*). Liquefaction in reverse density gradient systems has been identified before as a mechanism that forms downward-directed, soft-sediment deformation structures (*14*, *39*).

Seismic shaking is regarded as the most plausible triggering mechanism by far because of the lakes' proximity to seismic sources. Other mechanisms that could potentially lead to liquefaction, such as pressure fluctuations due to water waves and turbulent flow (*40*, *41*), tsunamis (*42*), rapid sediment loading (*43*), groundwater seepage (*44*), and periglacial processes (*45*), are not applicable to our study area. Hence, the load structures that occur in the tephra layers are referred to as tephra seismites (*20*). In environments subject to extensional tectonics, the process of passive sand infilling of fissures and cracks can result in the formation of downward-directed, soft-sediment deformation structures (*46*). However, we consider it improbable that fissures and cracks could form in soft, organic lake sediment because of its ductile deformation behavior. The likelihood of dewatering and shrinkage of mud as a factor contributing to the formation of the load structures is negligible, given that the lakes in the Hamilton lowlands have never dried out naturally (*47*).

The load structures exhibited variable dimensions between 0.4 and 35 cm. Some of the longer load structures intersected other underlying tephra layers (Fig. 2, B and C), indicating a high amount of energy release during the deformation process. Liquefaction did not appear to be limited by the thickness of the tephra layers (as noted earlier). We observed load structures in tephra layers as thin as 0.2 cm (data S1). Liquefaction in tephra layers has been reported before (*20*, *23*), but never has it been described in layers less than 1 cm thick.

We also observed other types of soft-sediment deformation structures, including collapsed tephra layers generated by the downward-directed emplacement of tephra material (Tu tephra in Fig. 2B and Rr tephra in Fig. 2D). At two lakes (HL and MH; see Fig. 1A), we observed several-decimeter-sized, upward-directed, plume-like, soft-sediment deformation structures. These occurred where normal density gradients prevailed over the sedimentary sequence, specifically at the interface between Late Pleistocene prelake volcanogenic alluvial deposits (dated at greater than approximately 20 cal ka B.P.) and organic lake sediments (fig. S4). These structures resulted from the fluidization and upward injection of liquefied coarse sand-sized, prelake volcanogenic alluvium into the low-density organic lake sediments, forming clastic dykes (*46*). The formation of these soft-sediment deformation structures has been widely observed during major earthquakes in New Zealand and elsewhere (*8*, *12*). In subsequent quantitative analyses of the occurrence and dimensions of tephra seismites, we did not further consider the collapse structures and clastic dykes because of the small sample size.

Interpolation maps for spatially assessing the occurrence and dimensions of liquefaction

The occurrence, morphological complexity, and dimensions of seismites have been shown to increase toward the seismic source (*48*, *49*). Our spatial liquefaction assessment is based on the quantification of

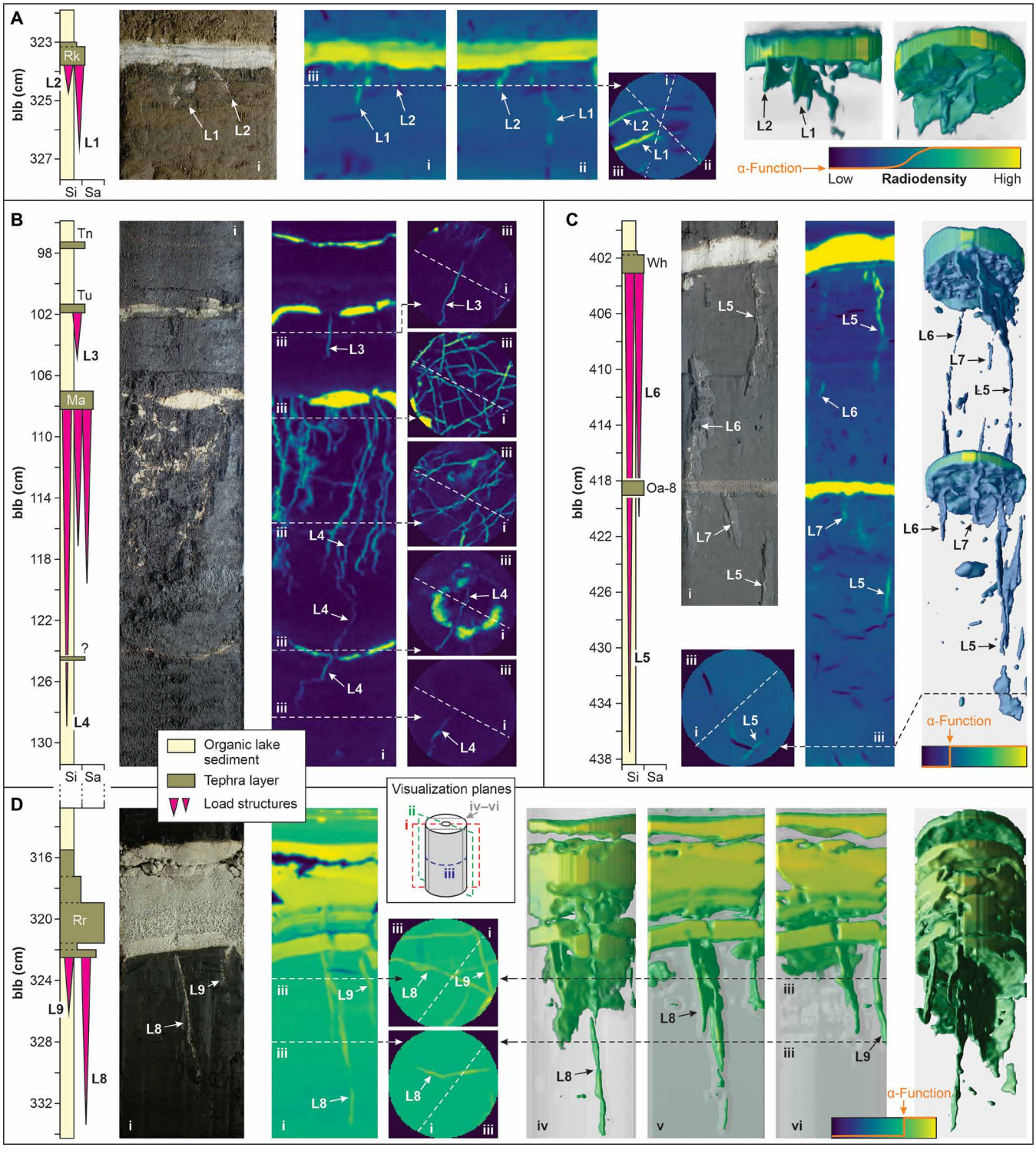

Fig. 2. Tephra seismites in the form of load structures of varying shapes and dimensions found in extant lake sediments in northern New Zealand. (**A**) Two intersecting load structures up to 3 cm long (designated liquefaction structures L1 and L2) beneath 0.8-cm-thick Rerewhakaaitu (Rk) tephra at Lake Rotomanuka (RM). (**B**) Multiple, complex load structures beneath 0.9-cm-thick Mamaku (Ma) tephra at Lake Mangahia (MH). One of the liquefaction structures (L4) intersects a 0.2-cm-thick unnamed tephra at 124-cm depth below the lake bottom (blb) and can be traced for more than 20 cm vertically. (**C**) Three straight load structures up to 34 cm long (L5 to L7) beneath the 1.6-cm-thick Waiohau (Wh) tephra at Lake Rotokaraka (RK), all of which are intersecting the 0.7-cm-thick Oa-8 tephra. (**D**) Two straight solitary liquefaction structures up to 11 cm long (L8 and L9) beneath the 7-cm-thick Rotorua (Rr) tephra at Lake Pikopiko (PP). Here, CT slices and volume slices (visualization planes: i, iv to vi) were used to provide insight into the liquefaction process: Liquefaction was triggered within the central medium sand bed of the Rr tephra at about 320 cm blb. Liquefied tephra material penetrated through the basal silt bed into the underlying organic lake sediment because of an inverse density gradient (*20*).

changes in the occurrence and dimensions of seismites within the Hamilton lowlands to locate areas with high liquefaction severity and, thus, high shaking intensity. The morphological complexity of tephra seismites was not taken into account in this study. We analyzed a total of 346 individual tephra layers via CT imaging, of which approximately one-third were classified as tephra seismite (see fig. S2 for details). The numbers of tephra layers and tephra seismites present at each lake are depicted in Fig. 3A. Tephra seismites were observed at all 18 lakes, with their quantity varying between lakes. This spatial variability is primarily attributed to two factors. The first is a variation in sample size between lakes, as the number of cores taken per lake ranged from 2 (e.g., lake PP) to 15 (at lake HL). Second, we expect the proximity to the seismic source to influence the observed quantity of tephra seismites (*49*). To remove the sample-size bias, leaving only an indication of proximity to seismic source, we normalized the number of tephra seismites by the total number of tephra layers at a given lake, yielding the seismite occurrence, *SO*, ratio. The seismite occurrence ratio was interpolated between lakes and shows that liquefaction structures are most common along a northeast trending transect from lakes in the southwest (MH and KM) through central lakes (HL and FL), to lake RK in the northeast of the study area (Fig. 3A). The mean seismite occurrence ratio (±1 SD) of lakes within this transect is $SO = 0.63 \pm 0.13$. However, the highest seismite occurrence ratio was identified at lake NI, located outside the transect, where more than 9 in 10 tephra layers ($SO = 0.92$) experienced liquefaction. Tephra seismites were much less prevalent at the remaining lakes ($SO = 0.17 \pm 0.07$).

The spatial liquefaction assessment was complemented by an assessment of variability in the dimensions of tephra seismites. First, the absolute dimensions of load structures were considered by grouping them threefold into small (<10 mm), intermediate (10 to 100 mm), and large (>100 mm) structures, the proportion of these size groups being demonstrated by the pie charts in Fig. 3B. In addition, the size of symbols in Fig. 3B denotes how many of the 14 prominent tephra layers liquefied, indicating the prevalence of liquefaction. The absolute dimensions of load structures are variable across the study area, and no clear trends could be observed for the three size groups. That is, some lakes with a low seismite occurrence ratio exhibited a high proportion of large load structures (e.g., at lake RI, having an *SO* ratio of 0.17, 50% of tephra seismites exhibited large load structures), whereas other lakes with high seismite occurrence ratios (e.g., lake HL) mainly exhibited intermediate load structures.

The absolute dimensions of seismites have limited meaning in paleoseismology because the dimensions of seismites depend on the volume of material available during the liquefaction process (*20*). Consequently, thicker tephra layers can generate longer deformation structures. The impact of tephra thickness on the dimensions of tephra seismites was eliminated through the integration of the length/thickness ratio, *LT*. The length/thickness ratio can be used to quantify the relative dimensions of individual seismites. For

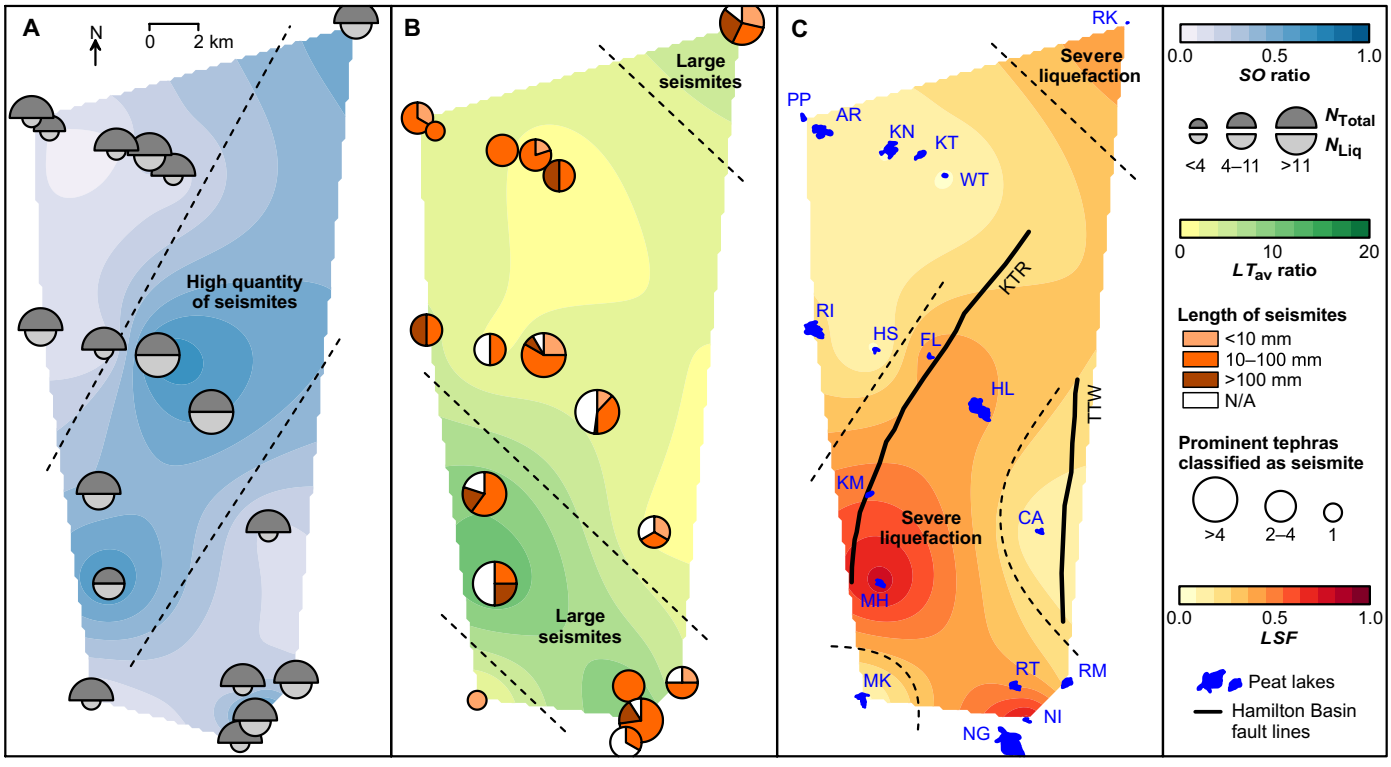

Fig. 3. Interpolation maps of liquefaction observations across the study area. (**A**) The seismite occurence, *SO*, ratio map shows how the quantity of tephra seismites varies spatially. Divided circles indicate the number of liquefied tephra layers and the total number of tephra layers analyzed at each lake. (**B**) The average length/thickness (LT_{av}) ratio map shows changes in the dimensions of tephra seismites. Colored pie charts show the proportion of tephra seismites grouped into vertical-length clusters of <1 cm, 1 to 10 cm, and >10 cm. The size of the pie charts symbolizes the number (how many) of the 14 prominent tephra layers from which the LT_{av} ratio was calculated. (**C**) The liquefaction severity factor, *LSF*, reflects the combined trends of the occurrence and dimensions of tephra seismites. Liquefaction severity is plotted together with the Kūkūtāruhe (KTR) and Te Tātua ō Wairere (TTW) faults in the Hamilton Basin.

example, tephra seismites illustrated in Fig. 2 exhibit length/thickness ratios ranging from 1.6 [liquefaction structure 8 (L8)] to 22.5 (L5). In the spatial liquefaction assessment, we averaged the length/thickness ratios for each lake (i.e., LT_{av} ratio) and interpolated those values across the Hamilton lowlands (Fig. 3B). The relative dimensions of tephra seismites increased toward the northeast, southwest, and southeast of the Hamilton lowlands. The average length/thickness ratio (±1 SD) of lakes within these areas is $LT_{av} = 8.4 \pm 3.0$, much higher than those of the remaining lakes ($LT_{av} = 2.0 \pm 0.9$).

The liquefaction severity factor, *LSF*, for each lake was calculated by averaging its seismite occurrence and average length/thickness ratios, and reflects the combined trends pertaining to both parameters (Fig. 3C). Analysis of the *LSF* interpolation map indicates three zones of severe liquefaction, characterized by frequent occurrence of large tephra seismites. These zones are believed to be associated with paleoearthquakes from three fault ruptures as follows. (i) An increase in liquefaction severity toward the northeast may be linked to near-field ground surface fault systems to the north and northeast (Fig. 1B). (ii) The high liquefaction severity along a northeast trending transect situated within the central region of the study area exhibits a strong correlation with the western Hamilton Basin fault named Kūkūtāruhe (KTR). Notably, higher levels of liquefaction severity were identified at the southern part of this fault. (iii) Liquefaction severity increases toward the southeast, which could indicate either a hidden, unmapped fault in this region or that the eastern Hamilton Basin fault, Te Tātua ō Wairere (TTW), extends further south and was active after the deposition of the tephra layers studied here.

Linking liquefaction to fault rupture through ground-shaking modeling

The final step in our paleoseismic analysis included determining the recurrence of paleoliquefaction (as a proxy for the recurrence of strong shaking in the area), comparing the timings of liquefaction with those of known fault ruptures, and inferring the recurrence intervals of paleoearthquakes on hidden or poorly known faults that have caused liquefaction in the study area.

Identifying seismic events SE1 to SE4

Our spatial analysis, using liquefaction parameters (*SO* ratio, LT_{av} ratio, and *LSF*) averaged over the entire stratigraphic sequence (Fig. 3), enabled the identification of three geographic zones of severe liquefaction. However, the analysis did not yield insights into the timing and recurrence interval of paleoearthquakes. The timing of paleoearthquakes that caused liquefaction in the study area is challenging to predict because the tephra layers are essentially unlithified, with no substantial diagenetic imprint to prevent (re)liquefaction from subsequent shaking (*20*). Consequently, liquefaction within our tephra layers could be the result of one or more seismic events that occurred after their deposition. However, subsequent seismic events have been hypothesized to increase the prevalence of tephra seismites (*15*), thereby increasing the likelihood of capturing deformation in sediment core. Therefore, we hypothesize that the seismite occurrence ratio will increase with age due to subsequent liquefaction events.

The temporal liquefaction assessment included an examination of how the occurrence of seismites of the 14 prominent tephra layers changed within the stratigraphic sequence (Fig. 4A). Each tephra was identified multiple times across the study area, with a typical frequency ranging from 15 to 40 instances. However, the thin Rm tephra was only identified on a limited number of occasions. The ages of the tephra layers exhibit a relatively even distribution within the stratigraphic sequence. The mean interval between tephra ages is 1.2 ± 0.8 cal ka. Average seismite occurrence ratios were obtained for the prominent tephra layers (except for Rm tephra), with these values being averaged over the study area (Fig. 4B). The occurrence of tephra seismites increased stepwise between Rr (15.7 cal ka B.P.) and Oa-8 (15.0 cal ka B.P.) tephras. The two oldest tephras (Rk and Rr) exhibited significantly higher levels of liquefaction compared with those of the younger tephras (Oa-8 to Tp). Although the two oldest tephras liquefied in ~66% of tephra layers ($SO = 0.66 \pm 0.02$), tephra seismites were identified only half as often in the younger tephras ($SO = 0.30 \pm 0.11$). The stepwise increase in the seismite occurrence indicates two seismic periods, referred to as SP1 and SP2. We infer from this analysis that the seismic period SP1 occurred between the deposition of Rr and Oa-8 tephras and that this period caused liquefaction in the two oldest tephras. The seismic period SP2 occurred subsequent to the deposition of Oa-8 tephra and resulted in seismites being generated in all tephra layers, including additional (re)liquefaction in the two oldest tephras. The additional liquefaction of the two oldest tephra layers (Rk and Rr) during seismic period SP2 explains why these have significantly higher seismite occurrences when compared with the occurrence associated with the younger tephra layers. The seismite occurrence ratio of the two oldest tephra layers is approximately twice as high as that obtained for the younger tephra layers. Consequently, we conclude that the two seismic periods induced comparable amounts of seismic energy in the study area, resulting in a similar number of new liquefaction structures within the sequence of tephra layers.

Two sets of interpolation maps were generated, one for each of the two seismic periods, to further investigate the location and timing of paleoliquefaction (Fig. 4, E and F). The two seismic periods are composed of four main seismic events, termed SE1 to SE4, each of which caused a geographically constrained zone of severe liquefaction. The extent of these zones is indicated by black dashed lines in Fig. 4 (E and F). The timing of seismic periods and seismic events is illustrated in Fig. 4D and summarized in table S3. The seismic period SP1 comprises a single seismic event SE1, which induced widespread liquefaction in the two oldest tephra layers (Rk and Rr) across the central and northeastern regions of the study area. The severity of liquefaction increases toward the northeast (Fig. 4E). No increase in liquefaction severity was observed along the Hamilton Basin faults, indicating that these were inactive during this seismic period. The relative dimensions of tephra seismites resulting from seismic event SE1 were found to be moderate, with length/thickness ratios typically ranging from 1 to 8 (Fig. 4C). Seismic event SE1 is well constrained in time by the notable stepwise increase in the seismite occurrence ratio between 15.7 and 15.0 cal ka B.P. (Fig. 4, B and D). The age of seismic event SE1 correlates with ruptures of the Kerepehi fault in the Hauraki Basin (see orange bar in Fig. 4D) (*29*).

The seismic period SP2 is composed of three seismic events (SE2 to SE4), as determined by the liquefaction severity distribution (Fig. 4F). The liquefaction caused by seismic events SE2 to SE4 is geographically more constrained than that due to seismic event SE1. The severity of liquefaction linked to seismic event SE2 increases toward the northeast, yet the extent of substantial liquefaction is less pronounced in comparison with that observed for the seismic event SE1 of the seismic period SP1. The SE2 event is only detectable in a single lake located at the northeast corner of the study area (RK; see inset map next to Fig. 4C). Tephras affected by the seismic event SE2 include the

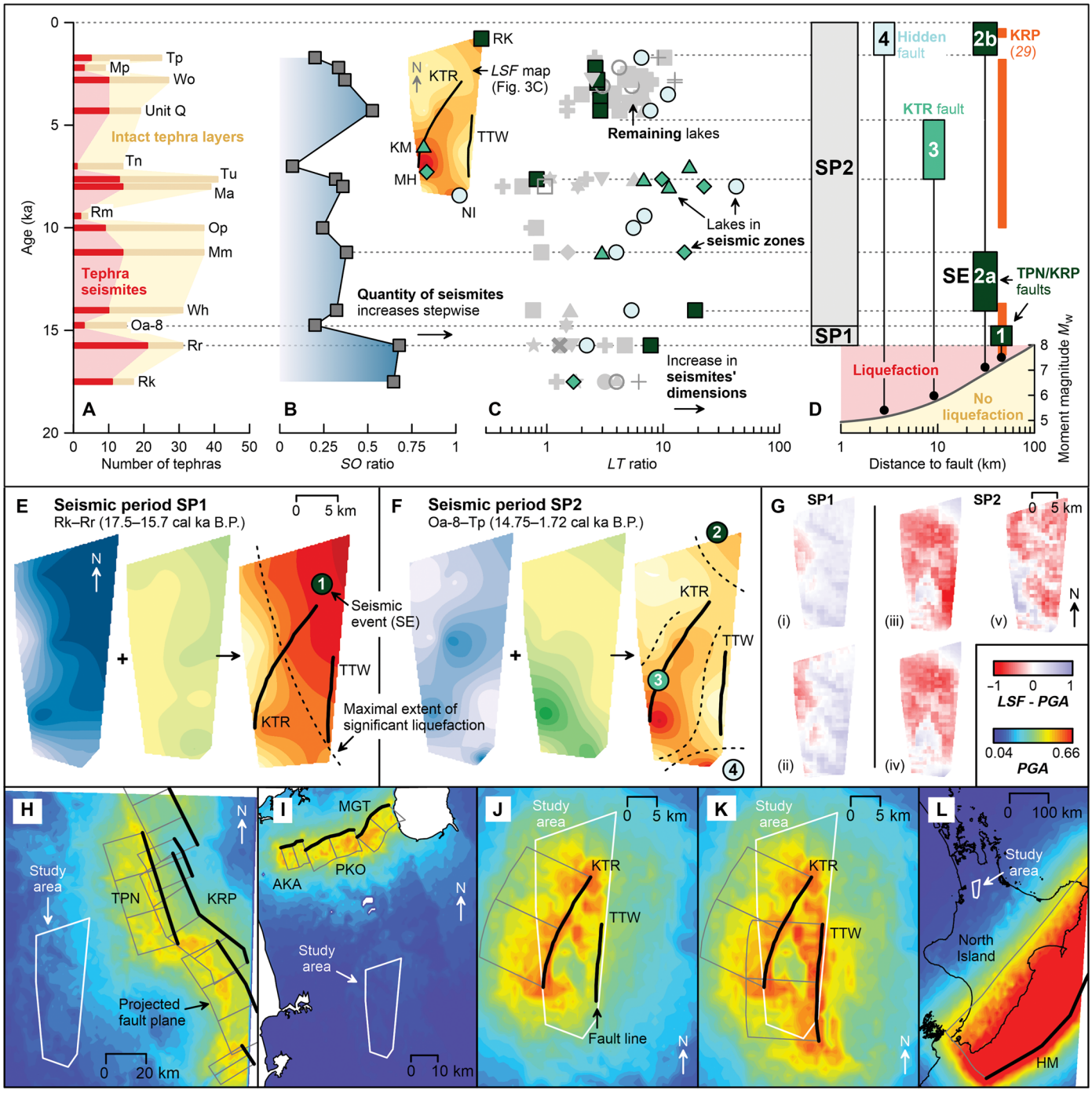

Fig. 4. Estimation of the locations, minimum M_w, and recurrence intervals of shaking from liquefaction maps. (**A**) Total number of tephra layers (yellow) and tephra seismites (red) for each of the 14 prominent tephra layers. (**B**) Seismic occurence ratio displayed against the age of tephra layers. A stepwise increase in seismite occurrence between Rr and Oa-8 tephras separates the two seismic periods (SP1 and SP2). (**C**) Length/thickness, *LT*, ratios of individual tephra seismites. Lakes highlighted in green and teal colors are located in one of the zones defined by seismic events SE2 to SE4 [inset *LSF* map to the left of (C)]. The highlighted lakes are underlain by all other lakes not located within one of the seismic zones (gray symbols). (**D**) Timing and minimum M_w of seismic events SE1 to SE4 obtained by estimating the distance between fault rupture and the most distal liquefaction observation in our study area [black dashed lines in (E) and (F)] following Maurer *et al.* (*51*). (**E** and **F**) Interpolation maps of the SO ratio, LT_{av} ratio, and *LSF* for each of the two seismic periods. (**G**) Model error maps of the rupture scenarios 1 to 5. The model error maps of rupture scenarios 1 and 2 were obtained from seismic period SP1, and model error maps of rupture scenarios 3 to 5 were obtained from seismic period SP2 (see fig. S5 and table S4 for further information). (**H** to **L**) *PGA* maps obtained from modeling of (H) the TPN-KRP fault rupture (M_w = 7.5) in the Hauraki Plains; (I) the AKA-PKO-MGT fault rupture (M_w = 7.3); (J) the KTR fault rupture (M_w = 7.15) and (K) the KTR-TTW fault rupture (M_w = 7.2), which are both in the Hamilton lowlands; and (L) the HM rupture (M_w = 9.1). Full lake and tephra names are provided in tables S1 and S2.

oldest tephra layer (Wh tephra, 14.0 cal ka B.P.) and the youngest tephra layers deposited during seismic period SP2 (Unit Q–Tp, 4.3 to 1.7 cal ka B.P.). These layers demonstrate moderate to high length/thickness ratios between 2.6 and 18 (Fig. 4C). Intermediate-aged tephras (Mm-Ma) remained unaffected, suggesting a hiatus in seismic activity. Consequently, we grouped the seismic event SE2 into two subevents SE2a and SE2b (Fig. 4D). The temporal constraints of both subevents are well defined. Specifically, SE2a occurs between the deposition of Wh and Mm tephras (14.0 to 11.3 cal ka B.P.) and SE2b after the deposition of Tp tephra (1.7 cal ka B.P.). The timing of seismic event SE2b corresponds to the activity of the Kerepehi fault (Fig. 4D) (*29*).

The seismic event SE3 is characterized by increased liquefaction severity along the western segment of the Hamilton Basin fault system, Kūkūtāruhe (KTR). Lakes affected by this seismic event include MH and KM, among others. In this region, tephra seismites were identified in Mm-Tn tephras (11.3 to 7.0 cal ka B.P.) and exhibited moderate to large dimensions (*LT* ratios of $7 \leq LT \leq 23$) (Fig. 4C). Subsequent tephras (Unit Q–Tp) remained unaffected by this event. Consequently, the occurrence of seismic event SE3 is well constrained and is likely to have occurred after Tn but before Unit Q tephras (7.0 to 4.3 cal ka B.P.) (Fig. 4D). The seismic event SE4 formed tephra seismites in the southeast corner of the study area. It is worth noting that at lake NI, almost all tephra layers of the seismic period SP2 liquefied, resulting in moderate to very large seismites (*LT* ratios of $2 \leq LT \leq 42$) (Fig. 4C). The seismic event SE4 occurred subsequent to the deposition of the youngest tephra layer in the lakes, Tp (1.7 cal ka B.P.) (Fig. 4D).

Identifying the faults that caused seismic events SE1 to SE4

The North Island of New Zealand is host to a considerable number of active faults, which have the potential to induce seismic shaking and, thus, liquefaction in the Hamilton lowlands (*30*). Here, we focused on the five most relevant rupture scenarios, which were selected on the basis of their activity, moment magnitude, and epicentral distance to the study area. The objective of this approach was to explain the liquefaction severity patterns caused by the seismic events SE1 to SE4 (table S4).

Seismic events SE1 and SE2 are accompanied by an increase in liquefaction severity toward the northeast. Two potential near-field (<100-km epicentral distance) rupture scenarios were identified, and the feasibility of associating them with the seismic events SE1 and SE2 was examined. The ground-shaking modeling of rupture scenario 1 incorporated the concurrent rupture of the Te Puninga (TPN) and Kerepehi (KRP) faults ($M_w = 7.5$), situated in the Hauraki Basin between 20 and 60 km to the northeast of the Hamilton lowlands (Fig. 4H). Scenario 1 resulted in substantial peak ground accelerations in the study area ($PGA_{max} = 0.53g$; table S5), which increased toward the northeast, replicating the liquefaction severity patterns of seismic events SE1 and SE2. Rupture scenario 2 incorporated the combined rupture of the Aka Aka (AKA), Pōkeno (PKO), and Mangatangi (MGT) faults, as well as the northern segment of Kerepehi ($M_w = 7.3$), situated between 60 and 90 km to the north of the study area (Fig. 4I). This scenario resulted in a substantially smaller peak ground acceleration compared with that of the first rupture scenario ($PGA_{max} = 0.38g$; table S5). The similarity between the liquefaction severity map and the peak ground acceleration obtained from the rupture scenarios was quantified by model error maps (Fig. 4G). The areas exhibiting the greatest similarity between observed liquefaction severity and modeled peak ground acceleration are indicated in white, whereas blue and red areas indicate a mismatch. A global error, defined as the sum of squared differences of the model error, was used to quantify the match between observed liquefaction severity and modeled peak ground acceleration. The model error obtained for rupture scenario 1 demonstrated a better match (i.e., a reduced proportion of blue and red areas) with the liquefaction severity of seismic events SE1 and SE2 compared with rupture scenario 2 (Fig. 4G). This improved match is supported by the observation that rupture scenario 2 exhibited a 32% higher global error (table S4). We conclude that seismic events SE1 and SE2 originated from a rupture of the Kerepehi–Te Puninga fault system.

Seismic event SE3 caused liquefaction of high severity along the western Hamilton Basin fault, Kūkūtāruhe (KRT). We considered two different rupture scenarios to test the high liquefaction severity along this fault. Rupture scenario 3, including only the Kūkūtāruhe fault ($M_w = 7.15$), caused widespread shaking in the central and western regions of the study area (Fig. 4J). In rupture scenario 4, both Hamilton Basin faults, Kūkūtāruhe and Te Tātua ō Wairere (TTW), were included ($M_w = 7.2$), thereby extending the seismic shaking further to the east (Fig. 4K). The shaking pattern of scenario 3 exhibits a stronger resemblance to the liquefaction severity map of seismic event SE3 than scenario 4, which has a 46% higher global error (table S4). We conclude that seismic event SE3 originated from a rupture of Kūkūtāruhe, partly located beneath what is now the urbanized area of Hamilton City.

Seismic event SE4 is characterized by high liquefaction severity in the southeast corner of the study area. There are no other active faults for more than 100 km to the southeast of Te Tātua ō Wairere. The nearest active fault with the potential to cause substantial seismic shaking in the study area is the Hikurangi Margin, located ~250 km to the southeast (*50*) (Fig. 1C). Ground-shaking modeling of the Hikurangi Margin (rupture scenario 5) yielded a high-magnitude earthquake ($M_w = 9.1$) that resulted in only negligible peak ground acceleration in the study area ($PGA_{max} = 0.19g$) (Fig. 4L and table S5). The model error map of rupture scenario 5 (Fig. 4G) displays a variable pattern with notable global error (table S4). The liquefaction severity of seismic event SE4 is very localized but at the same time shows high prevalence, that is, tephra seismites were observed in nearly all tephra layers (Fig. 4C). The localization and prevalence of liquefaction are indicative of a local seismic source. We conclude that the seismic event SE4 was caused by a near-field rupture of an unmapped, southern segment of the Te Tātua ō Wairere fault or a hidden (unknown) fault to the southeast of the study area.

Magnitudes of seismic events SE1 to SE4

We determined the minimum moment magnitudes of seismic events SE1 to SE4 by estimating the distance between fault rupture and the most distal liquefaction observation in our study area (black dashed lines in Fig. 4, E and F). Using the empirical relationship of Maurer *et al.* (*51*), we estimated minimum moment magnitudes of SE1 to SE4 strong enough to cause liquefaction in the tephra layers (Fig. 4D), ranging from ~7.4 (SE1) to ~5.2 (SE4). Minimum moment magnitudes estimated herein are comparable to moment magnitudes used in our ground-shaking modeling and to those obtained from the mapping of the active faults in the nearby Hauraki Plains (*28*, *29*). We acknowledge, however, that there is considerable uncertainty in applying the Maurer *et al.* (*51*) relationship, based on empirical information from liquefaction observations, to our tephra seismites, particularly with respect to liquefaction of relatively thin tephra layers encapsulated in the soft organic lake sediments in the Hamilton lowland lakes.

Applicability and limitations of tephra seismites in the area of paleoseismology

The novelty of our research is the development of a generic tool for investigating locations, recurrence intervals, and magnitudes of hidden faults or faults with poor surface expression. Our method combines the following: laboratory-based imaging of soft sediments in an environment with layers with high-density contrast; a solid spatial observation site distribution around the faults with no surface expression; and a previously unexplored liquefaction severity mapping approach that can be checked against ground-shaking maps from rupture of candidate sources.

In our study, we applied this method to thin distal lacustrine tephra layers younger than 20 cal ka B.P. in age preserved in organic lake sediment within extant lakes. This sedimentary environment brings many advantages for paleoseismology. For example, tephrochronology (and potentially radiocarbon dating) can be used to obtain precise age constraints and fine-grained, organic-bearing lake sediment provides favorable conditions for pore pressure buildup in thin siliciclastic layers. Following our approach, we were able to reconstruct the location and timing of at least five paleoearthquakes (SE1, SE2a, SE2b, SE3, and SE4) since 15.7 cal ka B.P., yielding a mean recurrence interval of ~3 ka. Furthermore, our method enabled the identification of an unmapped, hidden fault that has caused liquefaction in the southeast part of our study area since 1.7 cal ka B.P. We show strong evidence that the western Hamilton Basin fault, Kūkūtāruhe, being located directly underneath Hamilton City, was active within the ~15,700-year-long period covered in our study.

Our method is directly applicable in other volcanically active areas where tephra layers are embedded in lake sediments, such as Lake Riñihue, Chile (*25*) and Lake Torfdalsvatn, north Iceland (*23*). Our methodology is potentially applicable in many other volcanic/tectonic regions such as Mediterranean countries including Italy, as well as Japan, northwestern North America (Pacific Northwest, Alaska), various countries including Chile in South America, the East African Rift, and in central-eastern Europe, where faults occur amidst lakes containing liquefiable (medial to distal) tephra deposits.

The general method presented in our study is applicable to most sedimentary environments that allow for a high density contrast between layers. A high-density contrast is necessary to record liquefaction structures via CT imaging. Relevant environments include (i) lakes that contain event horizons, such as turbidites, mass transport deposits, sand laminations; (ii) lagoons and estuaries where storms and tsunamis have deposited thin granular layers into fine-grained sediment; and (iii) organic sag ponds next to faults (or caused by faulting) in areas distal to landslides or fault scarp–derived sediments. In those environments, our method would need to be modified to accommodate the different sediment sequences and sediment materials, among other factors. For example, if tephra layers or other chronostratigraphic marker horizons are not present, then cross-cutting relationships between liquefaction structures might provide age constraints. One study area where our approach could be readily adopted is the Green River Formation, Wyoming (*14*), where earthquake-induced, in situ liquefaction of different sizes was reported in laminated sandstone.

Our study in the Hamilton lowlands is limited, however, by available geological data comprising information from 18 locations (i.e., lakes) and from 14 isochronous time slices (i.e., tephra layers). The spatial and temporal dataset of liquefaction information is somewhat irregularly spaced, hence likely influencing the seismic hazard assessment. For example, lakes in the northern part of the study area (PP, AR, KN, KT, and WT) are more closely spaced than lakes in the central study area (RI, HS, FL, HL, KM, and CA). This phenomenon can potentially introduce bias in the spatial liquefaction interpolation maps, in turn influencing the identification of seismic sources. The quality of our temporal seismic assessment is governed by the distribution of tephra layers within the sediment record. In the event that tephra layers are absent from the sediment record or are spaced unevenly in time, the timing of seismic events will be less well constrained.

MATERIALS AND METHODS

Coring strategy

We cored 18 lakes from three different parts in the Hamilton lowlands: six in the north (PP, Pikopiko; AR, Areare; KN, Kainui; KT, Kaituna; WT, Whakatangi; RK, Rotokaraka); six in the center (RI, Rotokauri; HS, Horseshoe Lake/Waiwhakareke; FL, Forest Lake/Rotokaeo; HL, Hamilton Lake/Rotoroa; KM, Koromatua; CA, Cameron Lake/Kareaotahi); and six in the south (MH, Mangahia; MK, Mangakaware; NG, Ngaroto; NI, Ngarotoiti; RT, Ruatuna; RM, Rotomanuka) (Fig. 1A; see table S1 for further information on individual cores and sampling permits). Although there are 35 old (approximately 20 cal ka B.P.) blocked-valley riverine or riverine-phytogenic lakes in the Hamilton lowlands (*47*), the total number of lakes considered in this study was limited to 18 because of accessibility constraints (i.e., no permission to access the lake or dense vegetation or other problems preventing access to the lake shore). The average distance between neighboring lakes is 3.2 ± 2.5 km, with the smallest distance being between lakes PP and AR (i.e., 1.1 km) and the largest distance being between lakes RK and WT (i.e., 10.9 km). The 18 lakes encompass ~367 km^2 of the Hamilton lowlands (see dashed polygon in Fig. 1A), resulting in a lake frequency of ~1/20 km^2. The total number of lakes, average distance between lakes, and lake frequency considered in this study are unique when comparing the Hamilton lowlands with other study areas worldwide, where seismites have been used in paleoseismic investigations (*21*, *52*, *53*).

For each lake, one or more cores ~1.5 to 2 m in length were collected in 2016, 2020, and 2022 from partially overlapping sediment depths using a modified Livingstone piston corer with a 65- or 80-mm internal-diameter polyvinyl chloride core barrel (table S1). In most cases, cores were collected from the deepest basin(s) of the lakes, where the thickest and least disturbed sediments typically occur, and where the tephra-fall beds are essentially horizontal (*54*) and unaffected by other aseismic triggering mechanisms specific to other depositional environments, such as storm waves (*49*). In Lake Rotoroa/Hamilton Lake, seven coring sites were selected throughout the lake, including in shallow areas, whereas in most other lakes only one or two coring sites were selected. Where more than one core was required to capture the full sediment thickness in the lake, overlapping cores were taken and then accurately correlated using the stratigraphic superpositioning and distinctive physical properties of the glass-rich tephra layers present in the lake sediments, which typically vary in color and thickness (*27*, *55*, *56*), to produce a composite core ~3 to 5 m in length for each lake. An example of composite core construction using tephrostratigraphy can be found in the Supplementary Information of Kluger *et al.* (*20*).

In most lakes, duplicate cores were also collected from different locations within the lake basin. Because of the duplication and overlap of cores, most of the tephra layers could be investigated more

than once in each lake, increasing the confidence in the characterization of tephra layers and soft-sediment deformation structures. The tephra layers and stratigraphy of 10 lakes (Pikopiko, Areare, Kaituna, Whakatangi, Koromatua, Cameron Lake/Kareaotahi, Mangahia, Ruatuna, Rotomanuka, and Ngarotoiti) have not previously been described. The remaining eight lakes had been studied previously (*20*, *27*, *54*–*56*).

Visualization of tephra seismites by CT imaging

CT imaging of sedimentary structures in cores is a well-established technique in the natural sciences (*21*, *57*–*60*). It has been used previously to visualize soft-sediment deformation structures (*20*, *21*, *58*) but not to the extent reported herein. The CT scanner measures the attenuation of x-rays as they pass through different media. The amount of attenuation is mainly controlled by the density of the different media, making this technique very effective for studying three-dimensional features in organic-rich sediment cores.

CT imaging was performed using a medical CT scanner on 60 whole-round cores before opening (i.e., all lake cores except HL-A2 and HL-A3 from Rotoroa/Hamilton Lake, which were not available for CT imaging) to visualize and unambiguously quantify tephra layers and soft-sediment deformation structures. The whole-round core was positioned in the center of the CT table and preliminary scan results of the tephra layers and tephra seismites could be observed in the CT control room (fig. S1, A and B).

A CT stack (sequence of cross-sectional CT images) was generated for each core, with each CT image comprising voxels with dimensions of 0.625-mm depth and 0.684-mm width and height. The voxel values represent the radiodensity in Hounsfield units, *HU* (*61*). An *HU* value of −1000 represents the radiodensity of air, and an *HU* value of 0 represents the radiodensity of distilled water at standard temperature and pressure. CT image processing was performed using the public domain image processing software package ImageJ and its portable distribution Fiji (version 1.53t) and included the following steps (*62*):

1) Reduction of CT data: The raw CT stack initially consists of the core barrel (filled with sediment, water, and tephra) located longitudinally in the center of the CT table, both surrounded by air. To reduce computation time, the CT stack was roughly cropped to the data representing a cuboid around the core barrel using Fiji's rectangular selection tool.

2) Combination of CT stacks: Most of the sediment cores were short enough to be acquired in a single CT scan, but some of the longer cores extended beyond the measurement area of the medical CT scanner. For these cores, distinct layers were identified in the overview core scan, and CT imaging was then performed once from each core end, allowing the distinct layers to be recorded in both scans but in different directions. The reverse-direction CT scan was rotated 180° (using Fiji's rotation tool) and then combined with the first CT scan using the distinct layers as a reference.

3) Core rotation and realignment: Cores were sometimes not perfectly aligned longitudinally on the CT table. In addition, longer cores could not be placed flat on the CT table (because of a shelf space at the base of the CT table) and instead were slightly tilted upward at one end of the CT table, causing the core to be slightly rotated or bent upward, or both. The CT stacks were reoriented using Fiji's rotation tool. The curvature of the cores was removed using the open-source Fiji stack alignment plugin (*63*).

4) Removal of voxels outside the sediment core: After the core was properly rotated and aligned, the data representing the core barrel, CT table, and air were removed using Fiji's circular selection tool. The remaining CT stack represented only the inside of the core barrel (i.e., sediment, water, and tephra) in a cylindrical shape.

5) Contrast and brightness enhancement was applied to highlight the different sedimentary units in the core, mainly the organic lake sediment, tephra layers and soft-sediment deformation structures. The raw CT images that make up a CT stack use a standard linear transfer function between radiodensity and a grayscale value. Typically, black represents the lowest *HU* value (air), and white represents the highest *HU* value in the core. The sedimentary units in the core have relatively similar densities compared to that of the surrounding air, so the core appears white in the raw CT images (i.e., very little change in pixel values within the core) (first panel of fig. S1C). The contrast of CT images was enhanced using Fiji's enhance contrast tool. Voxel values were normalized to the highest value of the entire CT stack, with 0.35% of all voxels saturated (i.e., assigned a maximum value) (second panel of fig. S1C). A custom transfer function (mpl-viridis) was applied to the CT images to better highlight small density changes within tephra layers (third panel of fig. S1C). The custom transfer function assigns dark blue/purple to HU_{min}, green to $0.5HU_{max}$, and light yellow to HU_{max}.

6) Substacking: Stratigraphic units (i.e., tephra layers of known origin and age, organic lake sediment, and prelake alluvial sediment) were identified for each sediment core using information from the core description. Once the stratigraphic framework was established, substacks were created for the relevant tephra layers (Rk, Rr, Oa-8, Wh, Mm, Op, Rm, Ma, Tu, Tn, UnitQ, Wo, Mp, and Tp). In total, 346 tephra layers were visualized (fig. S2).

7) Visualization of CT substacks: Each substack, representing one or more tephra layers, was visualized in three ways (fig. S1D): (i) Longitudinal CT slices were generated through the center of the core. Typically, three longitudinal CT slices were generated at angles of 0°, 120°, and 240° (where 0° was defined as parallel to the cut core surface) to facilitate a systematic analysis of the vertical and horizontal extent of tephra layers and tephra seismites. Longitudinal CT slices were best suited to analyze the thickness of tephra layers as well as the maximum vertical length of soft-sediment deformation structures. (ii) A series of cross-sectional CT slices were generated for each CT stack containing tephra seismites to better visualize the changes in thickness and morphology of individual soft-sediment deformation structures with depth. Cross-sectional CT slices were used to assess the thickness and interconnectivity of individual soft-sediment deformation structures. (iii) Three-dimensional CT volumes were generated from each CT stack using Fiji's volume viewer plugin. The organic lake sediments above and below the tephra layers were digitally removed by applying an α-function based on x-ray attenuation, which was markedly different between the two constituents (i.e., organic lake sediments versus tephra) and allowed images to be exported showing only the tephra deposit. Standardized images were generated for each CT volume, including three images orthogonal to the core taken at angles of 0°, 120°, and 240° and two oblique images (one from above and one from below). CT volume images, in which the low-density organic lake sediment had been filtered out, provided the best tool for studying the three-dimensional morphology of the tephra seismite and tracking individual soft-sediment deformation structures. A compilation of all CT substack visualizations is provided in data S1.

Statistical analysis of tephra seismites

Statistical analysis was undertaken to quantify the extent of liquefaction throughout the study area. The severity of liquefaction is

considered to be related to the frequency and dimension of tephra seismites (*49*).

The frequency of tephra seismites at each lake was quantified by the seismite-occurrence ratio. Consequently, each individual tephra layer was classified into one of three types: (i) "seismites" (i.e., some type of soft-sediment deformation structure was identified, indicative of seismically induced liquefaction); (ii) "intact" (i.e., no post-depositional deformation of the tephra layer was identified); or (iii) "discontinuous" (i.e., the tephra layer exhibited some type of disruption that could not be definitively associated with any type of soft-sediment deformation structure), based on detailed sediment description of the opened cores and extensive examination of CT substacks (data S1). Discontinuous tephra layers were not considered further because of uncertainty about whether the disruption was caused by earthquake-induced liquefaction or other processes (e.g., coring, core splitting). Figure S2A provides a full account of the classification of tephra layers (i.e., seismites, intact, or discontinuous) considered in each sediment core and at each lake.

Then, the seismite-occurrence ratio *SO* was calculated (Eq. 1)

$$SO = N_{\text{Seismite}} / N_{\text{Total}} \quad (1)$$

where N_{Seismite} and N_{Total} are the number of tephra seismites and total tephra layers (i.e., the sum of intact tephra layers and tephra seismites), respectively. For example, consider a lake *X* where four overlapping cores were obtained (fig. S3A). The four cores contain a number of tephra layers (seven in this example) that could be correlated between cores using tephrostratigraphy. The tephra classification for this lake provides a distribution plot showing the number of intact tephra layers and tephra seismites for each of the seven tephra layers. For example, tephra layer number 4 occurs in three cores. It contains soft-sediment deformation structures in two of these instances and is intact in the other. The *SO* ratio of this particular example indicates that 38% of the tephra layers found at this lake were liquefied.

The dimensions of tephra seismites were analyzed by calculating the length/thickness ratio, *LT*, considering the maximum vertical length of the soft-sediment deformation structures normalized to the thickness of the tephra layer (fig. S3B). The maximum vertical length of the soft-sediment deformation structures was measured from the base of the tephra layer rather than from the central tephra bed in which liquefaction was initiated. This was because internal bedding could not be visualized for every tephra layer, particularly when tephra layers were thinner than the voxel resolution. For each tephra layer, the three longitudinal CT slices were used to obtain the maximum vertical length of the soft-sediment deformation structure, *L*, and the thickness of the tephra layers, *T*. Both parameters are the average of three values (one for each of the longitudinal CT slices). The *LT* ratio was then obtained (Eq. 2)

$$LT = L / T \quad (2)$$

In addition, average length/thickness ratios LT_{av} were obtained (Eq. 3)

$$LT_{\text{av}} = L_{\text{av}} / T_{\text{av}} \quad (3)$$

where L_{av} and T_{av} are the maximum vertical length of the soft-sediment deformation structures and tephra layer thickness, respectively, averaged over the entire lake. Figure S2B provides a full account of the *LT* ratio of tephra layers considered in each sediment core and in each lake.

The liquefaction severity factor *LSF* was introduced to examine the combined trends and patterns of *SO* and LT_{av} ratios within the study area and within the stratigraphic sequence (Eq. 4)

$$LSF = 0.5SO + 0.5\left(LT_{\text{av}} - LT_{\text{av,min}}\right) / \left(LT_{\text{av,max}} - LT_{\text{av,min}}\right) \quad (4)$$

The *LSF* is calculated by averaging the *SO* and LT_{av} ratios, the latter being normalized to the minimum and maximum values found across the study area. Normalization is necessary because *SO* and *LT* ratios have different dimensions. *SO* and *LT* ratios and *LSF* can also be calculated for subsets of tephra layers. For example, an LSF_{SP1} quantifies the liquefaction severity at a particular lake for the tephra layers deposited during the seismic period SP1.

The three liquefaction parameters, *SO* and *LT* ratios and *LSF*, were interpolated over the study area using a geographic information system (G.S. Surfer v. 19.2.213). The Kriging gridding algorithm was used as the interpolation method. Kriging is commonly used to interpolate between irregularly spaced data (*64*). The lakes in our study are somewhat irregularly spaced and therefore we used the default settings, which produce an accurate grid of the data. No anisotropy was applied to the gridding.

Ground motion modeling from fault rupture scenarios

Fault rupture geometries and characteristic magnitudes from New Zealand's Seismic Hazard Model (NZSHM22) (*65*) and the New Zealand Community Fault Model (*30*) were used to model ground motions for several fault rupture scenarios in the area of study. Peak ground acceleration, *PGA*, maps were calculated using OpenQuake (*66*) and the suite of ground motion prediction equations (GMPEs) recommended in NZSHM22 (*67*) for active crustal events. Site effects due to ground conditions were included using the time-averaged shear wave velocity model for the first 30 m of soil (Vs_{30}) from Foster *et al.* (*68*). Our ground motion estimations incorporate the notably low shear wave velocities typical of these deposits, with Vs_{30} values on the order of ~160 m/s. This value is consistent with the National Earthquake Hazards Reduction Program's Site Class E or F conditions and reflects amplification due to the presence of saturated, highly compressible nature of lacustrine organic-rich sediments. We acknowledge that empirical GMPEs based solely on Vs_{30} may underestimate *PGA* amplification in such soil conditions. Observational studies from events such as the 2011 Tohoku earthquake (*69*, *70*) have shown that in thick, saturated organic deposits, actual peak ground accelerations can exceed empirically predicted values by a factor of approximately 1.5 or more. However, we also recognize that there are documented cases where amplification in similar soft organic sediments has not been as pronounced as expected. For example, Bonilla *et al.* (*71*) reported modest amplification levels in peat-rich areas in the San Fernando Valley, despite low Vs_{30} values, attributed to strong nonlinear damping and limited energy trapping. In addition, other studies suggest that sediment thicknesses below ~10 m, particularly when composed of soft organic soils, may be insufficient to develop strong resonant amplification (*72*, *73*).

The North Island of New Zealand hosts a large number of active faults that potentially could have caused seismic shaking in the Hamilton lowlands (*30*). An initial review of all potential faults produced five main fault rupture combinations by means of activity, moment magnitude, and epicentral distance to the study area. For this study, we considered the following fault rupture combinations: (i) Te Puninga and Kerepehi faults ($M_{\text{w}} = 7.5$); (ii) Aka Aka, Pōkeno,

Mangatangi, and the northern segment of Kerepehi ($M_w = 7.3$); (iii) Kūkūtāruhe ($M_w = 7.15$); (iv) Kūkūtāruhe and Te Tātua ō Wairere ($M_w = 7.2$); and (v) a M_w-9.1-Hikurangi Margin earthquake. Rupture geometries were converted to a format suitable for OpenQuake, and the modeling was performed using scenario analysis, where the rupture geometry and the selected magnitude are used to estimate ground motions from the GMPEs for a defined number of simulations to capture the associated uncertainties. Mean ground motion values were extracted for each fault rupture combination from 1000 simulations in a 500-m-resolution grid and were used in further analyses.

The similarity between the liquefaction severity distributions and the *PGA* distributions from fault rupture modeling was quantified by a model error, *ME* (Eq. 5)

$$ME = LSF - \left(PGA_{\max} - PGA\right) / \left(PGA_{\max} - PGA_{\min}\right) \quad (5)$$

where *LSF* and *PGA* are the grids of the liquefaction severity factor and peak ground acceleration, respectively, the latter being normalized to the minimum and maximum values of the *PGA* grid. Equation 5 produces model error grids that can be used to see whether the spatial pattern of liquefaction severity matches that obtained from seismic shaking modeling at site (Fig. 4G and fig. S5). A global error (sum of squared differences) was calculated from the model error grids and was used to quantify the similarity between the maps (Eq. 6)

$$\mathrm{SSD} = \sum_{i=0}^{n} \left(ME_i\right)^2 \quad (6)$$

where *i* denotes the individual points of the model error grid. Model error grids and sum of squared differences were generated for both seismic periods and for each seismic rupture scenario (fig. S5 and table S4).

Supplementary Materials

This PDF file includes:

Figs. S1 to S5
Tables S1 to S5
Data S1
References

REFERENCES

1. J. F. Dolan, S. A. Christofferson, J. H. Shaw, Recognition of paleoearthquakes on the Puente Hills blind thrust fault, California. *Science* **300**, 115–118 (2003).
2. L. M. Liberty, M. A. Hemphill-Haley, I. P. Madin, The Portland Hills Fault: Uncovering a hidden fault in Portland, Oregon using high-resolution geophysical methods. *Tectonophysics* **368**, 89–103 (2003).
3. B. H. Mackey, M. C. Quigley, Strong proximal earthquakes revealed by cosmogenic 3He dating of prehistoric rockfalls, Christchurch, New Zealand. *Geology* **42**, 975–978 (2014).
4. J. H. Shaw, P. M. Shearer, An elusive blind-thrust fault beneath metropolitan Los Angeles. *Science* **283**, 1516–1518 (1999).
5. I. J. Hamling, S. Hreinsdóttir, K. Clark, J. Elliott, C. Liang, E. Fielding, N. Litchfield, P. Villamor, L. Wallace, T. J. Wright, E. D'Anastasio, S. Bannister, D. Burbidge, P. Denys, P. Gentle, J. Howarth, C. Mueller, N. Palmer, C. Pearson, W. Power, P. Barnes, D. J. A. Barrell, R. Van Dissen, R. Langridge, T. Little, A. Nicol, J. Pettinga, J. Rowland, M. Stirling, Complex multifault rupture during the 2016 M_w 7.8 Kaikōura earthquake, New Zealand. *Science* **356**, eaam7194 (2017).
6. R. Stone, A Bengali recipe for disaster. *Science* **332**, 1256–1258 (2011).
7. J. Moernaut, J. Howarth, K. Kremer, K. Wils, "Lacustrine records of past seismic shaking" in *Understanding Past Earthquakes*, A. Elliott, C. Gruetzner, Eds. (Springer, 2025), pp. 169–227.
8. S. F. Obermeier, N. R. Bleuer, C. A. Munson, P. J. Munson, W. S. Martin, K. M. McWilliams, D. A. Tabaczynski, J. K. Odum, M. Rubin, D. L. Eggert, Evidence of strong earthquake shaking in the lower Wabash Valley from prehistoric liquefaction features. *Science* **251**, 1061–1063 (1991).
9. M. P. Tuttle, L. W. Wolf, M. E. Starr, P. Villamor, R. H. Lafferty III, J. E. Morrow, R. J. Scott Jr., S. L. Forman, K. Hess, K. Tucker, Evidence for large New Madrid earthquakes about AD 0 and 1050 BC, central United States. *Seismol. Res. Lett.* **90**, 1393–1406 (2019).
10. M. Moretti, A. Ronchi, Liquefaction features interpreted as seismites in the Pleistocene fluvio-lacustrine deposits of the Neuquén Basin (northern Patagonia). *Sediment. Geol.* **235**, 200–209 (2011).
11. H. El Taki, B. R. Pratt, Syndepositional tectonic activity in an epicontinental basin revealed by deformation of subaqueous carbonate laminites and evaporites: Seismites in Red River strata (Upper Ordovician) of southern Saskatchewan, Canada. *Bull. Can. Pet. Geol.* **60**, 37–58 (2012).
12. P. Villamor, P. Almond, M. P. Tuttle, M. Giona-Bucci, R. M. Langridge, K. Clark, W. Ries, S. H. Bastin, A. Eger, M. Vandergoes, Liquefaction features produced by the 2010–2011 Canterbury earthquake sequence in southwest Christchurch, New Zealand, and preliminary assessment of paleoliquefaction features. *Bull. Seismol. Soc. Am.* **106**, 1747–1771 (2016).
13. K. Mueller, J. Champion, M. Guccione, K. Kelson, Fault slip rates in the modern New Madrid seismic zone. *Science* **286**, 1135–1138 (1999).
14. B. Törő, B. R. Pratt, Sedimentary record of seismic events in the Eocene Green River Formation and its implications for regional tectonics on lake evolution (Bridger Basin, Wyoming). *Sediment. Geol.* **344**, 175–204 (2016).
15. M. A. Rodríguez-Pascua, V. H. Garduño-Monroy, I. Israde-Alcántara, R. Pérez-López, Estimation of the paleoepicentral area from the spatial gradient of deformation in lacustrine seismites (Tierras Blancas Basin, Mexico). *Quat. Int.* **219**, 66–78 (2010).
16. H. L. Hilbert-Wolf, E. L. Simpson, W. S. Simpson, S. E. Tindall, M. C. Wizevich, Insights into syndepositional fault movement in a foreland basin; trends in seismites of the Upper Cretaceous, Wahweap Formation, Kaiparowits Basin, Utah, USA. *Basin Res.* **21**, 856–871 (2009).
17. M. Sintubin, "Archaeoseismology: Identifying earthquake effects in ancient sites" in *Understanding Past Earthquakes*, A. Elliott, C. Gruetzner, Eds. (Springer, 2025), pp. 81–97.
18. J. Chaneva, M. O. Kluger, V. G. Moon, D. J. Lowe, R. P. Orense, Monotonic and cyclic undrained behaviour and liquefaction resistance of pumiceous, non-plastic sandy silt. *Soil Dyn. Earthq. Eng.* **168**, 107825 (2023).
19. J. Chaneva, M. O. Kluger, T. Ilanko, V. G. Moon, D. J. Lowe, R. P. Orense, Using undrained cyclic triaxial tests to examine liquefaction resistance of historically liquefied pumiceous volcanic-ash soil materials and back-estimate prehistoric earthquakes. *Eng. Geol.* **354**, 108131 (2025).
20. M. O. Kluger, D. J. Lowe, V. G. Moon, J. Chaneva, R. Johnston, P. Villamor, T. Ilanko, R. A. Melchert, R. P. Orense, R. C. Loame, N. Ross, Seismically-induced down-sagging structures in tephra layers (tephra-seismites) preserved in lakes since 17.5 cal ka, Hamilton lowlands, New Zealand. *Sediment. Geol.* **445**, 106327 (2023).
21. A. Molenaar, M. Van Daele, T. Vandorpe, G. Degenhart, M. De Batist, R. Urrutia, M. Pino, M. Strasser, J. Moernaut, What controls the remobilization and deformation of surficial sediment by seismic shaking? Linking lacustrine slope stratigraphy to great earthquakes in south–central Chile. *Sedimentology* **68**, 2365–2396 (2021).
22. K. Monecke, F. S. Anselmetti, A. Becker, M. Schnellmann, M. Sturm, D. Giardini, Earthquake-induced deformation structures in lake deposits: A Late Pleistocene to Holocene paleoseismic record for Central Switzerland. *Eclogae Geol. Helv.* **99**, 343–362 (2006).
23. D. J. Harning, C. R. Florian, Á. Geirsdóttir, T. Thordarson, G. H. Miller, Y. Axford, S. Ólafsdóttir, High-resolution Holocene record from Torfdalsvatn, north Iceland, reveals natural and anthropogenic impacts on terrestrial and aquatic environments. *Clim. Past Discuss.* **21**, 795–815 (2025).
24. Y. Lu, N. Wetzler, N. Waldmann, A. Agnon, G. P. Biasi, S. Marco, A 220,000-year-long continuous large earthquake record on a slow-slipping plate boundary. *Sci. Adv.* **6**, eaba4170 (2020).
25. A. Molenaar, M. Van Daele, J.-J. S. Huang, M. Strasser, M. De Batist, M. Pino, R. Urrutia, J. Moernaut, Disentangling factors controlling earthquake-triggered soft-sediment deformation in lakes. *Sediment. Geol.* **438**, 106200 (2022).
26. D. J. Lowe, Tephrochronology and its application: A review. *Quat. Geochronol.* **6**, 107–153 (2011).
27. D. J. Lowe, Stratigraphy, age, composition, and correlation of late Quaternary tephras interbedded with organic sediments in Waikato lakes, North Island, New Zealand. *N. Z. J. Geol. Geophys.* **31**, 125–165 (1988).
28. P. Villamor, K. Clark, G. Coffey, J. Hughes, D. J. Lowe, A. Hogg, V. Moon, J. Moratalla, K. Thingbaijam, The Te Puninga Fault, Hauraki Plains: A new seismic source in the low seismicity northern region of New Zealand. *N. Z. J. Geol. Geophys.* **68**, 609–627 (2025).
29. M. Persaud, P. Villamor, K. R. Berryman, W. Ries, J. Cousins, N. Litchfield, B. V. Alloway, The Kerepehi Fault, Hauraki Rift, North Island, New Zealand: Active fault characterisation and hazard. *N. Z. J. Geol. Geophys.* **59**, 117–135 (2016).
30. H. Seebeck, R. V. Dissen, N. Litchfield, P. M. Barnes, A. Nicol, R. Langridge, D. J. A. Barrell, P. Villamor, S. Ellis, M. Rattenbury, The New Zealand Community Fault Model–version 1.0: An improved geological foundation for seismic hazard modelling. *N. Z. J. Geol. Geophys.* **67**, 209–229 (2024).

31. D. Kear, J. C. Schofield, Geology of the Ngaruawahia subdivision. *N.Z. Geol. Survey Bull* **88**, 1–168 (1978).
32. B. V. Alloway, D. J. Lowe, B. J. L. Jensen, G. Plunkett, "Tephrochronology", in *The Encyclopedia of Quaternary Science, Third Edition*, S. A. Elias, Ed. (Elsevier, 2025), vol. 5, pp. 780–838.
33. G. Owen, Load structures: Gravity-driven sediment mobilization in the shallow subsurface. *Geol. Soc. Lond. Spec. Publ.* **216**, 21–34 (2003).
34. J. P. Calvo, M. Rodriguez-Pascua, S. Martin-Velazquez, S. Jimenez, G. D. Vicente, Microdeformation of lacustrine laminite sequences from Late Miocene formations of SE Spain: An interpretation of loop bedding. *Sedimentology* **45**, 279–292 (1998).
35. N. Eyles, B. M. Clark, Gravity-induced soft-sediment deformation in glaciomarine sequences of the Upper Proterozoic Port Askaig Formation, Scotland. *Sedimentology* **32**, 789–814 (1985).
36. A. R. Fortuin, C. J. Dabrio, Evidence for Late Messinian seismites, Nijar Basin, south-east Spain. *Sedimentology* **55**, 1595–1622 (2008).
37. A. T. Martel, M. R. Gibling, Clastic dykes of the Devono-Carboniferous Horton Bluff Formation, Nova Scotia: Storm-related structures in shallow lakes. *Sediment. Geol.* **87**, 103–119 (1993).
38. J. Chaneva, M. O. Kluger, V. G. Moon, D. J. Lowe, R. P. Orense, in *Proceedings of the 7th International Young Geotechnical Engineers Conference*, Scott, Ed. (Australian Geomechanics Society, 2022), pp. 313–318.
39. B. R. Pratt, J. J. Ponce, Sedimentation, earthquakes, and tsunamis in a shallow, muddy epeiric sea: Grinnell Formation (Belt Supergroup, ca. 1.45 Ga), western North America. *Geol. Soc. Am. Bull.* **131**, 1411–1439 (2019).
40. S. Dzuynski, A. J. Smith, Convolute lamination, its origin, preservation, and directional significance. *J. Sediment. Res.* **33**, 616–627 (1963).
41. S. Okusa, Wave-induced stresses in unsaturated submarine sediments. *Geotechnique* **35**, 517–532 (1985).
42. B. E. Benson, K. A. Grimm, J. J. Clague, Tsunami deposits beneath tidal marshes on northwestern Vancouver Island, British Columbia. *Quatern. Res.* **48**, 192–204 (1997).
43. J. M. Anketell, J. Cegła, S. Dżułyński, On the deformational structures in systems with reversed density gradients. *Ann. Soc. Geol. Pol.* **40**, 3–30 (1970).
44. Y. Li, J. Craven, E. S. Schweig, S. F. Obermeier, Sand boils induced by the 1993 Mississippi River flood: Could they one day be misinterpreted as earthquake-induced liquefaction? *Geology* **24**, 171–174 (1996).
45. C. Harris, J. Murton, M. C. R. Davies, Soft-sediment deformation during thawing of ice-rich frozen soils: Results of scaled centrifuge modelling experiments. *Sedimentology* **47**, 687–700 (2002).
46. M. Moretti, L. Sabato, Recognition of trigger mechanisms for soft-sediment deformation in the Pleistocene lacustrine deposits of the Sant'Arcangelo Basin (southern Italy): Seismic shock vs. overloading. *Sediment. Geol.* **196**, 31–45 (2007).
47. D. J. Lowe, J. D. Green, "Origins and ages" in *The Hidden Gems of the Waikato—The History, Ecology and Management of the Waikato Lakes—Ō Tātou Roto: He Taonga Tuku Iho*, D. Özkundakci, N. Grainger, T. Dean-Speirs, Eds. (Waikato Regional Council and the Environmental Research Institute, University of Waikato, 2025), pp. 9–53.
48. M. C. Pope, J. F. Read, R. Bambach, H. J. Hofmann, Late Middle to Late Ordovician seismites of Kentucky, southwest Ohio and Virginia: Sedimentary recorders of earthquakes in the Appalachian basin. *Geol. Soc. Am. Bull.* **109**, 489–503 (1997).
49. G. Owen, M. Moretti, Identifying triggers for liquefaction-induced soft-sediment deformation in sands. *Sediment. Geol.* **235**, 141–147 (2011).
50. K. Clark, J. Howarth, N. Litchfield, U. Cochran, J. Turnbull, L. Dowling, A. Howell, K. Berryman, F. Wolfe, Geological evidence for past large earthquakes and tsunamis along the Hikurangi subduction margin, New Zealand. *Mar. Geol.* **412**, 139–172 (2019).
51. B. W. Maurer, R. A. Green, M. C. Quigley, S. Bastin, Development of magnitude-bound relations for paleoliquefaction analyses: New Zealand case study. *Eng. Geol.* **197**, 253–266 (2015).
52. J. Moernaut, M. Van Daele, K. Heirman, K. Fontijn, M. Strasser, M. Pino, R. Urrutia, M. De Batist, Lacustrine turbidites as a tool for quantitative earthquake reconstruction: New evidence for a variable rupture mode in south central Chile. *J. Geophys. Res. Solid Earth* **119**, 1607–1633 (2014).
53. M. Strasser, K. Monecke, M. Schnellmann, F. S. Anselmetti, Lake sediments as natural seismographs: A compiled record of Late Quaternary earthquakes in central Switzerland and its implication for alpine deformation. *Sedimentology* **60**, 319–341 (2013).
54. D. J. Lowe, Application of impulse radar to continuous profiling of tephra-bearing lake sediments and peats: An initial evaluation. *N. Z. J. Geol. Geophys.* **28**, 667–674 (1985).
55. J. D. Green, D. J. Lowe, Stratigraphy and development of c. 17 000 year old Lake Maratoto, North Island, New Zealand, with some inferences about postglacial climatic change. *N. Z. J. Geol. Geophys.* **28**, 675–699 (1985).
56. D. J. Lowe, Using soil stratigraphy and tephrochronology to understand the origin, age, and classification of a unique Late Quaternary tephra-derived Ultisol in Aotearoa New Zealand. *Quaternary* **2**, 1–34 (2019).
57. A. Tanaka, T. Nakano, K. Ikehara, X-ray computerized tomography analysis and density estimation using a sediment core from the Challenger Mound area in the Porcupine Seabight, off western Ireland. *Earth Planets Space* **63**, 103–110 (2011).
58. Y. Nakashima, J. Komatsubara, Seismically induced soft-sediment deformation structures revealed by X-ray computed tomography of boring cores. *Tectonophysics* **683**, 138–147 (2016).
59. W. K. Hamblin, X-ray radiography in the study of structures in homogeneous sediments. *J. Sediment. Res.* **32**, 201–210 (1962).
60. T. H. Orsi, C. M. Edwards, A. L. Anderson, X-ray computed tomography: A nondestructive method for quantitative analysis of sediment cores. *J. Sediment. Res.* **64**, 690–693 (1994).
61. G. N. Hounsfield, Computerized transverse axial scanning (tomography): Part 1. Description of system. *Br. J. Radiol.* **46**, 1016–1022 (1973).
62. S. J. Brookes, "Using ImageJ (Fiji) to analyze and present X-ray CT images of enamel" in *Odontogenesis: Methods and Protocols*, P. Papagerakis, Ed. (Springer New York, 2019), pp. 267–291.
63. Q. Tseng, E. Duchemin-Pelletier, A. Deshiere, M. Balland, H. Guillou, O. Filhol, M. Théry, Spatial organization of the extracellular matrix regulates cell–cell junction positioning. *Proc. Natl. Acad. Sci. U.S.A.* **109**, 1506–1511 (2012).
64. R. M. Pokhrel, J. Kuwano, S. Tachibana, A kriging method of interpolation used to map liquefaction potential over alluvial ground. *Eng. Geol.* **152**, 26–37 (2013).
65. M. C. Gerstenberger, S. Bora, B. A. Bradley, C. DiCaprio, R. J. Van Dissen, G. M. Atkinson, C. Chamberlain, A. Christophersen, K. J. Clark, G. L. Coffey, C. A. D. L. Torre, S. M. Ellis, J. Fraser, K. Graham, J. Griffin, I. J. Hamling, M. P. Hills, A. Howell, A. Hulsey, J. Hutchinson, P. Iturrieta, K. M. Johnson, V. O. Jurgens, A. E. Kaiser, R. Kirkham, R. M. Langridge, R. L. Lee, N. J. Litchfield, E. F. Manea, J. Maurer, K. R. Milner, A. Nicol, S. J. Rastin, M. S. Rattenbury, D. A. Rhoades, J. Ristau, C. Rollins, H. Seebeck, B. Shaw, J. Townend, D. Schorlemmer, P. J. Stafford, M. W. Stirling, K. K. S. Thingbaijam, P. Villamor, L. M. Wallace, G. Weatherill, C. A. Williams, L. M. Wotherspoon, "New Zealand National Seismic Hazard Model 2022 revision: Model, hazard and process overview" (GNS Science Report 2022/57, GNS Science, 2022).
66. GEM, Golbal Earthquake Model (2019); https://hazard.openquake.org/gem/results/.
67. B. Bradley, S. Bora, R. Lee, E. F. Manea, M. Gerstenberger, P. J. Stafford, G. M. Atkinson, G. Weatherill, J. Hutchinson, C. de la Torre, "Summary of the ground-motion characterisation model for the 2022 New Zealand National Seismic Hazard Model" (GNS Science Report 2022/46, GNS Science, 2022).
68. K. M. Foster, B. A. Bradley, C. R. McGann, L. M. Wotherspoon, AVS 30 map for New Zealand based on geologic and terrain proxy variables and field measurements. *Earthq. Spectra* **35**, 1865–1897 (2019).
69. H. Kawase, K. Aki, A study on the response of a soft basin for incident S, P, and Rayleigh waves with special reference to the long duration observed in Mexico City. *Bull. Seismol. Soc. Am.* **79**, 1361–1382 (1989).
70. J. P. Stewart, E. Seyhan, D. M. Boore, NGA-West2 equations for predicting PGA, PGV, and 5%-damped PSA for shallow crustal earthquakes. *Earthq. Spectra* **30**, 1057–1085 (2014).
71. L. F. Bonilla, J. H. Steidl, G. T. Lindley, A. G. Tumarkin, R. J. Archuleta, Site amplification in the San Fernando Valley, California: Variability of site-effect estimation using the S-wave, coda, and H/V methods. *Bull. Seismol. Soc. Am.* **87**, 618–630 (1997).
72. D. Roten, D. Fäh, K. B. Olsen, D. Giardini, A comparison of observed and simulated site response in the Rhône valley. *Geophys. J. Int.* **173**, 958–978 (2008).
73. C. Cornou, P.-Y. Bard, M. Dietrich, Contribution of dense array analysis to the identification and quantification of basin-edge-induced waves, Part I: Methodology. *Bull. Seismol. Soc. Am.* **93**, 2604–2623 (2003).
74. G. J. Leonard, J. G. Begg, C. J. N. Wilson, "Geology of the Rotorua area: Scale 1:250,000" *1:250,000 geological map 5. 1 sheet and 99p* (Institute of Geological and Nuclear Sciences, 2010).
75. A. G. Hogg, T. F. Higham, D. J. Lowe, J. G. Palmer, P. J. Reimer, R. M. Newnham, A wiggle-match date for Polynesian settlement of New Zealand. *Antiquity* **77**, 116–125 (2003).
76. D. J. Lowe, M. Blaauw, A. G. Hogg, R. M. Newnham, Ages of 24 widespread tephras erupted since 30,000 years ago in New Zealand, with re-evaluation of the timing and palaeoclimatic implications of the Lateglacial cool episode recorded at Kaipo bog. *Quat. Sci. Rev.* **74**, 170–194 (2013).
77. A. Hogg, D. J. Lowe, J. Palmer, G. Boswijk, C. B. Ramsey, Revised calendar date for the Taupo eruption derived by ^{14}C wiggle-matching using a New Zealand kauri ^{14}C calibration data set. *Holocene* **22**, 439–449 (2012).
78. A. Hogg, C. Wilson, D. J. Lowe, C. Turney, P. White, A. Lorrey, S. Manning, J. Palmer, S. Bury, J. Brown, J. Southon, F. Petchey, Wiggle-match radiocarbon dating of the Taupo eruption. *Nat. Commun.* **10**, 4669 (2019).
79. S. B. Piva, S. J. Barker, N. A. Iverson, V. H. L. Winton, N. A. Bertler, M. Sigl, C. J. Wilson, N. W. Dunbar, A. V. Kurbatov, L. Carter, Volcanic glass from the 1.8 ka Taupō eruption (New Zealand) detected in Antarctic ice at ~ 230 CE. *Sci. Rep.* **13**, 16720 (2023).
80. D. J. Lowe, A. B. H. Rees, R. M. Newnham, Z. J. Hazell, M. J. Gehrels, D. J. Charman, M. J. Amesbury, Isochron-informed Bayesian age modelling for tephras and cryptotephras: application to mid-Holocene Tuhua tephra, northern New Zealand, in

Book of Abstracts, Crossing New Frontiers: INTAV International Field Conference on Tephrochronology, "Tephra Hunt in Transylvania", U. Hambach, D. Veres, Eds. Moieciu de Sus, Romania, 24 June to 1 July 2018, pp. 95–96.
81. L. Peti, K. E. Fitzsimmons, J. L. Hopkins, A. Nilsson, T. Fujioka, D. Fink, C. Mifsud, M. Christl, R. Muscheler, P. C. Augustinus, Development of a multi-method chronology spanning the Last Glacial Interval from Orakei maar lake, Auckland, New Zealand. *Geochronol. Discuss.* **2020**, 1–54 (2020).
82. L. Peti, J. L. Hopkins, P. C. Augustinus, Revised tephrochronology for key tephras in the 130-ka Ōrākei Basin maar core, Auckland Volcanic Field, New Zealand: Implications for the timing of climatic changes. *N. Z. J. Geol. Geophys.* **64**, 235–249 (2021).
83. W. Topping, Tephrostratigraphy and chronology of late Quaternary eruptives from the Tongariro Volcanic Centre, New Zealand. *N. Z. J. Geol. Geophys.* **16**, 397–423 (1973).
84. P. C. Froggatt, D. J. Lowe, A review of late Quaternary silicic and some other tephra formations from New Zealand: Their stratigraphy, nomenclature, distribution, volume, and age. *N. Z. J. Geol. Geophys.* **33**, 89–109 (1990).
85. C. J. N. Wilson, Stratigraphy, chronology, styles and dynamics of late Quaternary eruptions from Taupo volcano, New Zealand. *Philos. Trans. R. Soc. Lond. A. Math. Phys. Eng. Sci.* **343**, 205–306 (1993).
86. M. Heinrich, S. J. Cronin, N. Pardo, Understanding multi-vent Plinian eruptions at Mt. Tongariro volcanic complex, New Zealand. *Bull. Volcanol.* **82**, 30 (2020).
87. I. A. Nairn, T. Kobayashi, M. Nakagawa, The ~10 ka multiple vent pyroclastic eruption sequence at Tongariro Volcanic Centre, Taupo Volcanic Zone, New Zealand: Part 1. Eruptive processes during regional extension. *J. Volcanol. Geotherm. Res.* **86**, 19–44 (1998).
88. S. Donoghue, V. Neall, A. Palmer, Stratigraphy and chronology of late Quaternary andesitic tephra deposits, Tongariro Volcanic Centre, New Zealand. *J. R. Soc. N. Z.* **25**, 115–206 (1995).
89. A. Auer, C. Martin, J. Palin, J. White, M. Nakagawa, C. Stirling, The evolution of hydrous magmas in the Tongariro Volcanic Centre: The 10 ka Pahoka-Mangamate eruptions. *N. Z. J. Geol. Geophys.* **58**, 364–384 (2015).
90. S. Donoghue, R. Stewart, A. Palmer, Morphology and chemistry of olivine phenocrysts of Mangamate tephra, Tongariro Volcanic Centre, New Zealand. *J. R. Soc. N.Z.* **21**, 225–236 (1991).
91. D. J. Lowe, thesis, University of Waikato, Hamilton, New Zealand (1987).
92. S. L. Donoghue, thesis, Massey University, Palmerston North, New Zealand (1991).
93. S. Donoghue, V. Neall, Tephrostratigraphic studies at Tongariro volcanic centre, New Zealand: An overview. *Quat. Int.* **34**, 13–20 (1996).
94. S. J. Cronin, V. E. Neall, A. S. Palmer, Investigation of an aggrading paleosol developed into andesitic ring-plain deposits, Ruapehu volcano, New Zealand. *Geoderma* **69**, 119–135 (1996).
95. A. G. Hogg, D. J. Lowe, C. H. Hendy, University of Waikato radiocarbon dates I. *Radiocarbon* **29**, 263–301 (1987).
96. A. G. Hogg, T. J. Heaton, Q. Hua, J. G. Palmer, C. S. Turney, J. Southon, A. Bayliss, P. G. Blackwell, G. Boswijk, C. B. Ramsey, SHCal20 Southern Hemisphere calibration, 0–55,000 years cal BP. *Radiocarbon* **62**, 759–778 (2020).
97. P. Shane, L. R. Doyle, I. A. Nairn, Heterogeneous andesite–dacite ejecta in 26–16.6 ka pyroclastic deposits of Tongariro Volcano, New Zealand: The product of multiple magma-mixing events. *Bull. Volcanol.* **70**, 517–536 (2008).

Acknowledgments: We thank iwi of Ngāti Wairere (especially H. Broadhurst and W. Puke) and Ngā Iwi Tōpū O Waipā (especially H. Coromandel-Wander), staff of Hamilton City Council, Waipā and Waikato district councils, the Department of Conservation, and private land owners for their ongoing support in providing access to lakes for coring and in other ways. M. Vandergoes, S. Wood, A. Rees, and H. Gard, representing the Lakes380 project, are thanked for sediment coring in 2020 and 2022 (Vandergoes and Rees also undertook coring in 2016); Hamilton Radiology for providing CT scanning facilities; A. Harpur and R. Loame for helping to describe sediment cores in 2016; V. Gibbons and J. Hughes for field and laboratory assistance; R. Johnston (Swansea University) for supporting initial CT imaging; A. Lorrey and J.-M. Woolley (NIWA) for the application of ground-penetrating radar to Hamilton Lake/Rotoroa; R. Liefting for Waikato Regional Council funding support; S. Lovatt, C. Robinson, M. Barbour, and I. McDonald (all Waikato University) for administrative support relating to funding; and M. Chivers and Y. Chen and the Library Open Access Equity Fund of the University of Waikato. **Funding:** This study was supported by Marsden Fund grant UOW1902 of the Royal Society Te Apārangi (D.J.L., M.O.K., V.G.M., P.V., R.P.O., R.A.M., J.M.M., T.I., and J.C.); Ministry of Business, Innovation and Employment (MBIE) Endeavour Fund (Smart Ideas) grant UOWX1903 (D.J.L., M.O.K., V.G.M., P.V., R.P.O., R.A.M., J.M.M., T.I., and J.C.); Earthquake Commission (EQC) grant 15/U713 (D.J.L.); Earthquake Commission (EQC) grant BIG 012 2020 (P.V. and D.J.L.); University of Waikato SIF research grant 2016 (D.J.L.); PhD fees-scholarship grant provided by the Waikato Regional Council (J.C.); Ministry of Business, Innovation and Employment (MBIE) Strategic Science Investment Fund (GNS-Hazards and Risk Management Programme) (P.V.); and NZ Centre for Earthquake Resilience (QuakeCoRE) (R.P.O.). **Author contributions:** Conceptualization: M.O.K., D.J.L., and V.G.M. Methodology: M.O.K., R.A.M., J.M.M., D.J.L., and J.C. Investigation: M.O.K., R.A.M., J.M.M., T.I., N.R., J.C., D.J.L., and V.G.M. Visualization: M.O.K. and R.A.M. Funding acquisition: D.J.L., M.O.K., V.G.M., P.V., and R.P.O. Project administration: M.O.K., D.J.L., and T.I. Supervision: D.J.L., V.G.M., M.O.K., and R.P.O. Data curation: M.O.K., N.R., and R.A.M. Validation: M.O.K. and J.M.M. Formal analysis: M.O.K., J.C., J.M.M., P.V., R.P.O., R.A.M., and T.I. Software: M.O.K., N.R., J.M.M., and R.A.M. Writing—original draft: M.O.K. and J.M.M. Writing—review and editing: M.O.K., D.J.L., J.M.M., P.V., T.I., R.P.O., V.G.M., and J.C. **Competing interests:** The authors declare that they have no competing interests. **Data, code, and materials availability:** All data and code needed to evaluate and reproduce the results in the paper are present in the paper and/or the Supplementary Materials. Medical CT data in its native format are available at https://doi.org/10.5061/dryad.5x69p8dj9. Sediment core logs/photos are available upon request to M.O.K. (mkluger@posteo.de). Sediment cores have been returned to lakes to fulfil requirements of mana whenua partners Ngā Iwi Toopu o Waipā.

Submitted 2 August 2024
Accepted 16 January 2026
Published 18 February 2026
10.1126/sciadv.ads2015

ScienceAdvances

Tephra seismites—Understanding seismic hazard of hidden faults by analyzing liquefied tephra layers in lakes

Max O. Kluger, Richard A. Melchert, José M. Moratalla, Tehnuka Ilanko, David J. Lowe, Vicki G. Moon, Pilar Villamor, Jordanka Chaneva, Nic Ross, and Rolando P. Orense

Sci. Adv. **12** (8), eads2015. DOI: 10.1126/sciadv.ads2015